Photoemission from doped solid rare gases*

Zohar Ophir, Baruch Raz, and Joshua Jortner

Department of Chemistry, Tel Aviv University, Tel Aviv, Israel

Volker Saile, Nikolaus Schwentner, Ernst-Eckhard Koch†, Michael Skibowski, and Wulf Steinmann

Sektion Physik der Universität München, München, Germany
(Received 29 August 1974)

In this paper we report the results of an experimental study of the photoelectric yield of doped solid rare gases in the extreme ultraviolet ($h\omega$ = 8–30 eV) spanning the range of impurity excitations, exciton states, and interband transitions. Results were obtained for Xe in Kr, Xe in Ar, Kr in Ar, and benzene in Ar, Kr, and Xe. For dilute atomic and molecular impurities in solid rare gases three intrinsic photoemission mechanisms are exhibited: (a) direct excitation from the impurity state above the impurity threshold, (b) electronic energy transfer from the host exciton states to the impurity states resulting in exciton induced impurity photoemission, and (c) direct photoemission from the host matrix at energies above the matrix threshold. The photoemission thresholds from impurity states via processes (a) or (b) result in detailed information regarding electron affinities of solid rare gases which are in good agreement with recent data for the pure solids. A detailed study of exciton induced photoemission was conducted on Xe/Ar mixtures. The energy dependent photoemission line shape at different film thicknesses and at different concentrations was analyzed in terms of a kinetic picture involving competition between energy transfer from "free" excitons and exciton trapping. A quantitative estimate of the diffusion length of Wannier excitons in solid Ar was extracted.

1. INTRODUCTION

The optical properties of solid rare gases have attracted considerable interest in the past few years both from the theoretical[1] and the experimental[2] points of view. The electronic energy levels of these large gap insulators have been extensively studied by absorption and reflection spectroscopy, elucidating the nature of exciton states and interband transitions in these systems. Recent measurements of the photoelectric yield from pure rare gas solids provided additional information on the location of the vacuum level, the scattering of photoexcited electrons, and the decay of excitons.[3–5] It is of interest to extend these investigations to study photoemission from doped solid rare gases. In the present paper we report the results of an experimental study of the photoemission yield in the energy range 8–30 eV from doped solid rare gases using dilute rare gas alloys Xe in Kr, Xe in Ar, Kr in Ar, and a molecular impurity, i.e., benzene in Ar, Kr, and Xe. The goals of this investigations have been twofold. First, additional information can be obtained from photoemission studies from dilute impurity states in solid rare gases on the electron affinities of these solids. These data will be complementary to those obtained from the experiments[3,4] on the pure solids. Second, and more interesting, photoemission from mixed solids provides a powerful tool for the study of exciton dynamics in solid rare gases by monitoring exciton induced impurity photoemission originating from electron energy transfer from the "free" exciton levels to the impurity states.[6]

The energy V_0 of the bottom of the conduction band relative to the vacuum level, i.e., $V_0 \equiv -E_A$, in a solid rare gas, serves as an indicator for the delicate balance between the repulsive and the attractive interactions exerted on an electron by the solid, and is of considerable theoretical interest. Quite reliable information is available on the energy required for electron injection into liquid He,[7a] liquid Ne (e.g. Refs. 7b, 7c), and liquid Ar[7d] and on electron mobilities in the liquid rare gases. However, the extension of these techniques for the corresponding solids is fraught with difficulties due to electrode solid interface effects and electron backscattering corrections. Spectroscopic data for the low lying Wannier series in solid rare gases and in dilute rare gas alloys yield the band gap E_g for the pure solid and the impurity band gap E_g^i for the impurity states. Independently E_g has been determined recently from photoconductivity measurements for liquid Xe[8] in agreement with the value determined from the Wannier series. The impurity band gap E_g^i is related to V_0 by

$$E_g^i = I_g^i + P_+^i + V_0 , \tag{1.1}$$

where I_g^i is the impurity gas phase ionization potential and P_+^i is the polarization energy of the medium by the positive hole. Theoretical estimates of P_+ together with experimental values of E_g^i were utilized for an estimate of V_0. The direct method for obtaining V_0 in solid rare gases involves a combination of photoemission threshold values (E_{TH} and E_{TH}^i) for the pure solid and for the impurity state, respectively, and spectroscopic data for E_g or E_g^i, whereupon

$$V_0 = E_g - E_{TH} \quad \text{for the pure solid} \tag{1.2a}$$

or

$$V_0 = E_g^i - E_{TH}^i \quad \text{for the impurity state.} \tag{1.2b}$$

Photoemission yield curves for pure solid rare gases and for some atomic and molecular impurity states were recently reported and analyzed according to Eq. (1.2). In the present paper we present the results of a detailed study of the photoemission thresholds in doped solid rare gases which yield further reliable information regarding the V_0 values.

Physical information concerning exciton dynamics in

simple insulators such as solid rare gases is of considerable interest. The vacuum ultraviolet luminescence spectra of pure solid Ar, Kr, and Xe exhibit the emission from electronically excited, vibrationally relaxed rare gas diatomic molecules, which result from an efficient exciton trapping process.[9] Medium perturbations of the diatomic molecule are minor.[9,10] No emission could be detected from exciton states in these solids.[10,11] Thus, from the exciton radiative lifetime $\tau_r \simeq 10^{-9}$ sec (estimated from the integrated oscillator strength), we infer that exciton trapping occurs within $\tau_0 < \tau_r/100 \simeq 10^{-11}$ sec. Relevant information regarding exciton dynamics can be obtained from experimental studies of photoemission resulting from electronic energy transfer from bound Wannier excitons to some impurity states in solid rare gases.[6] Now the lowest bound Wannier exciton states of the matrix, characterized by the energy levels E_n ($n = 1, 2, \ldots$), can be located either above or below E^i_{TH}. In the former case, i.e. $E_n > E^i_{TH}$ (for all n), direct photoemission from impurity states will be observed in the energy range $E^i_{TH} \leq E \leq E_1$. In the latter case, when $E_1 \leq E^i_{TH}$, one can expect photoemission due to energy transfer to the impurity from free exciton states (those such that $E_n \geq E^i_{TH}$). It is important to emphasize that this Auger-type impurity ionization process can result only from the "collision" of a free exciton with the impurity. The electronic energy E_m of the trapped exciton[9,10,12] (that is the diatomic molecule) is too low, i.e. $E_m \leq E^i_{TH}$ to induce impurity ionization (see Fig. 1). A dramatic enhancement of the photoemission yield of Xe lightly doped with benzene and in Xe/Kr (doping level ~1%) was observed[6] when excited into the exciton bands of the host crystal. These results provide direct information pertaining to exciton dynamics in solid Xe and Kr, and provided an estimate for the exciton diffusion length in solid Xe. Exciton induced photoemission in solid rare gases bears a close analogy to photoemission from alkali halides containing F centers.[13] However, in the former case the effect provides information regarding free exciton dynamics on the time scale $\tau \approx 10^{-11}$–10^{-12} sec[12] prior to exciton trapping.

In summary, three extrinsic photoemission mechanisms can be observed for dilute atomic and molecular impurity states in solid rare gases:

(a) direct excitation of the impurity state above E^i_{TH};

(b) electronic energy transfer from the host matrix Wannier states, E_n ($n = 1, 2\ldots$) located at $E_n \geq E^i_{TH}$ to the impurity resulting in exciton induced impurity photoemission;

(c) at energies above E_{TH}, direct photoemission from the host matrix is exhibited.

These processes constitute the subject of the present study.

2. EXPERIMENTAL TECHNIQUES

2.1 Apparatus

In this work we have employed two types of experimental setups. The one limited to the "low" energy range of 6–11.5 eV while the second spanned the high energy region of 9–35 eV.

2.1.1. *Low energy experiments*

The vacuum ultraviolet light source consisted of a high pressure (2–5 atm) high intensity gas pulsed discharge lamp.[14] The light source emits a train of pulses, the pulse width being 2 μsec, with a repetition rate which could be varied in the range 10–250 pulses/sec. The light was passed through a 0.3 m Czerny–Turner monochromator (McPherson 218) with a grating blazed at 1500 Å, employing a spectral resolution of 5 Å (~0.025 eV). The monochromator was separated from the sample chamber by a LiF window. The optical arrangement allowed for a simultaneous measurement of optical absorption and photoemission yield. The emitter electrode consisted of a 3 mm wide gold strip evaporated on a LiF window. The collector electrode was a gold ring of 15 mm diameter, located 30 mm from the emitter. The signal was amplified by a differential amplifier (Brookdeal–9432) followed by a low noise amplifier (Brookdeal–450) and finally amplified and integrated by a Boxcar integrator (Brookdeal) which was triggered by the same electrical pulse used for the lamp triggering. In this way a noise level of 5×10^{-18} A was achieved for the measurement of the photoelectric current. The samples were prepared by deposition of a gaseous mixture on the emitter electrode mounted on a variable temperature helium flow cryostat at 40 °K for Xe samples, at 30 °K for Kr samples, and 20 °K for Ar samples. These temperatures provided well annealed films. The gaseous mixtures were prepared and handled in an UHV system previously pumped down to less than 10^{-9} torr. The sample chamber was pumped by an ion pump and a cryogenic pump down to less than 10^{-9} torr.

2.1.2 *High energy experiments*

The photon energy range 9–35 eV was spanned with the continuous synchrotron radiation of the electron accelerator DESY. Details of the apparatus used will be

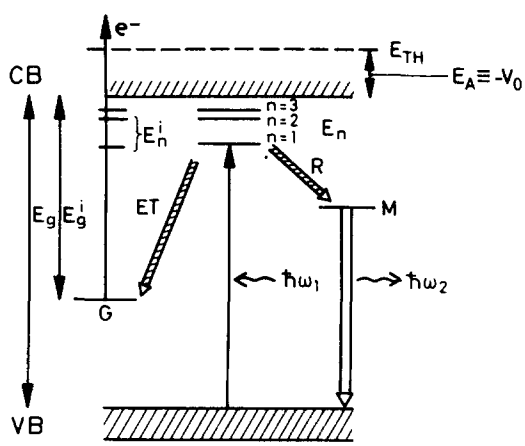

FIG. 1. Schematic scheme of the energy levels involved in photoelectron emission from doped solid rare gases. VB valence band, CB conduction band, E_{TH} vacuum level, V_0 electron affinity ($\equiv -E_A$), E_n exciton states of the host matrix, E^i_n exciton states of the impurity, M trapped exciton states of the host matrix, G impurity state of the guest atoms or molecules. The arrows indicate the various processes discussed in the text.

given elsewhere.[15] Measurements were made with an ultrahigh vacuum system for combined optical and photoemission measurements in the extreme vacuum ultraviolet at pressures lower than 5×10^{-10} torr. Light was admitted into the sample chamber through the exit slit of a normal incidence monochromator,[16] which served as part of a differential pumping unit against the base pressure in the synchrotron beam line and in the monochromator, where the pressure was in the 1×10^{-7} torr range. The samples were prepared *in situ* by condensing the rare gases as thin films onto a cryogenically cooled gold substrate. The low temperatures for solidifying the rare gases were obtained with the aid of a bakeable, liquid He flow cryostat with two radiation shields (see Fig. 2). This cryostat offers the additional advantages of a rotatable sample holder as well as the possibility to tilt the sample in order to achieve optimum alignment with respect to the light beam. The reflectance at normal incidence could be measured with an open electrostatic photomultiplier simultaneously with the yield. The samples could be removed out of the light beam for the determination of the incident photon flux with the same photomultiplier.

Yield spectra were measured by a continuous scan of the incident photon energy with a resolution of 2 Å over the whole spectral range from 9 to 35 eV. Photoelectrons from the samples were collected by a plane copper mesh of 75% light transmittance in front of the emitting surface with an electric field of 2000 V/cm to insure saturation of the photocurrent.

2.1.3. Determination of film thickness

As has been shown earlier, photoemission from solid rare gases is dependent on the film thickness of the samples.[4b] In the present investigation the thickness dependence of the line shapes of the yield curves shall be discussed. To this end the film thickness of the samples was determined in the "low" energy experiment from the oscillations of the transmittance and in the "high" energy experiment from those of the reflectance observed simultaneously for visible and uv light with increasing thickness during the evaporation. The accuracy of the values for the thickness given with our results amounts to ± 10 Å.

2.2 Determination of photoemission yields

Photoemission measurements on insulators are hampered by sample charging.[3] This problem was minimized by measuring the yield spectra of thin films or for low sample currents.

For the determination of the absolute yield per incident photon the absolute intensity of the incoming photon flux was measured with a Samson double ionization chamber placed at the exit slit of the monochromator. The values thus obtained were further checked by comparing them to the measured photo current of the gold coated substrate before evaporation of the rare gas films.

In order to obtain quantitative values for the yield from the samples, the measured yield curves (Y_m) were corrected for the reflectance from the vacuum sample interface as well as for a structureless contribution from second order light from the monochromator (Y_2) (≈ 3% of 20 eV intensity at 10 eV):

$$Y_c = (Y_m - Y_2)/(1 - R), \tag{2.1}$$

where R is the reflectance of the sample–substrate

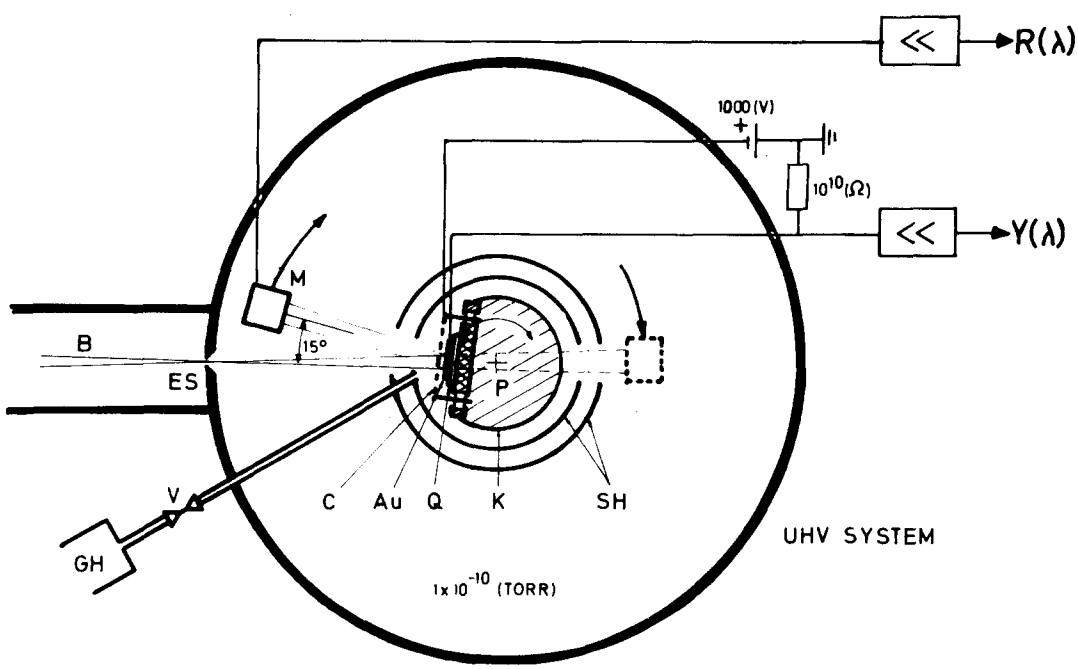

FIG. 2. Experimental arrangement for the simultaneous measurement of photoemission yield and reflectance spectra at liquid He temperatures in the photon energy range 9–35 eV. *B* light beam from the monochromator, *ES* exit slit, *M* photomultiplier, *K* cryostat, *SH* shields, *P* pivot, *Q* quartz substrate, Au gold film, *C* copper mesh, *GH* gas handling system, *V* needle valve.

combination measured simultaneously with the yield for each individual sample.

For spectral ranges outside the regions of strong absorption of the samples (e.g. below the first exciton) one observes a contribution to the photoyield, due to hot electrons excited at the gold substrate, which travel through the rare gas film and escape into the vacuum. It is worth noting that this hot electron contribution to the yield is an interesting phenomenon in itself. It gives information about the scattering length of electrons photoinjected into the rare gas. The energy loss of electrons emitted from the gold substrate was studied in the low energy setup by investigating the thickness dependence of the yield in the spectral range where the sample is optically transparent. A quantitative assessment of the hot electron contribution in our experiments is, however, not easy because a precise knowledge of the light intensity at the gold substrate is necessary for a detailed investigation of the phenomenon.

We are interested in the yield spectra from the rare gas samples. Therefore, we have roughly separated the hot electron contribution by subtracting from the yield Y_c the contribution from the Au substrate Y_{Au}. For Y_{Au} we used the gold yield, taking into account the simultaneously determined reflectance from the sample-Au sandwich but neglecting the absorption within the sample. The corrected yields are thus taken as $Y = Y_c - Y_{Au}$.

2.3 Samples

An ultrahigh vacuum gas handling system was used for the preparation of the samples. The purity of the rare gases from L' Air Liquide and Matheson research grade was $\geq 99.9997\%$, $\geq 99.9999\%$ for Ar, $\geq 99.997\%$, $\geq 99.995\%$ for Kr, and $\geq 99.997\%$ for Xe, respectively. They were used without further attempts for purification. Between gases of different suppliers no difference for the results could be stated. Sample composition was controlled by mixing the appropriate amounts of the constituents in the gas handling system; the amounts were controlled by measuring the total pressure. These mixtures were evaporated at temperatures below the sublimation temperature of both constituents. The composition of the samples given with our results refers to the relative partial pressures of the total pressure of 1000 torr in the gas handling system. Ideal mixing as well as equal sticking coefficients for the various components of a mixture have to be assumed, if this is regarded as the true sample composition.

The speed of evaporation could be varied by a needle valve. Typical values used were 2–25 Å/sec.

We shall frequently refer to the photoelectric yield spectra from "pure" samples. In order to get an estimate for the changes which impurities would cause in the spectra, yield spectra from rare gases doped with N_2, O_2, and CH_4 have been investigated during the course of the present experiment. In any case the features discussed below were not affected by this doping. The reason for this is the fact that in view of their high ionization potential, the energy gap E_g^i of these impurities is so large that they cannot contribute effectively to photoemission.

2.4 Spectroscopic data

When reflectance spectra are presented together with the photoemission curves, the former refer to the spectra measured for the particular sample studied. It should be noted that these reflectance spectra should not be used for a deduction of optical constants, because for these thin films strong interference effects are still present. This particular aspect of the rare gas films has been, on the other hand, exploited to deduce optical constants from the change of reflectance with film thickness or, if the optical constants are known, to determine the film thickness of a particular sample.[17,18] Absorption coefficients for Ar have been taken from a careful reinvestigation of the optical constants in the excitonic range[19] and those for Kr and Xe from the available absorption spectra.[20] The data handling system used to process the spectroscopic data is described elsewhere.[21]

3. EXPERIMENTAL RESULTS

We shall now proceed to present the experimental data for the energy dependence of the photoemission curves, $Y(E)$, from lightly doped solid rare gases. For all systems studied the energy dependent photoelectric yield was found to vary with sample thickness d and with the concentration $[R]$ of rare gas guest atoms. These features will be discussed in detail for the Xe doped Ar films. For the other systems typical spectra are presented. The photoemission onsets are independent of d and $[R]$. Experimentally there exists, however, a lower limit for the concentration and thickness of the films which can be investigated, since a minimal amount of absorption is required in order to obtain a clearly detectable onset of the yield.

3.1 Impurity states in krypton

3.1.1. Xenon in krypton

In Fig. 3 we present the photoelectric yield spectrum for 1% Xe in Kr. For the sake of comparison the yield spectrum of undoped Kr[4a] as well as the reflectance from the doped sample are shown. The values for the energy gap of Kr as obtained from optical experiments (e.g. Ref. 2) $E_g = 11.58$ eV as well as the threshold energy $E_{TH} = 11.9$ eV are marked by arrows. The curves which have been corrected as described in Sec. II represent the relative yields per photon penetrating into the sample. Above 13 eV both curves reach values for the yield of ~50%.

The yield from the Xe in Kr system has been recently studied also by Ophir *et al.*[6] up to energies of 11.2 eV. In Fig. 4 the two spectra are compared and we notice that below 10 eV there is fair agreement between the two experiments. The strong onset of emission at 10.3 eV is only indicated as a small dip and subsequent shoulder in the previous experiment.

The source of the discrepancy between the result presented here for Xe/Kr and that previously obtained[6] is due to the very low absorption coefficient k at the threshold energy around 10.3 eV. In the work of Ophir *et al.*[6] thin films were used and as mentioned above it is difficult under these conditions, to observe the onset

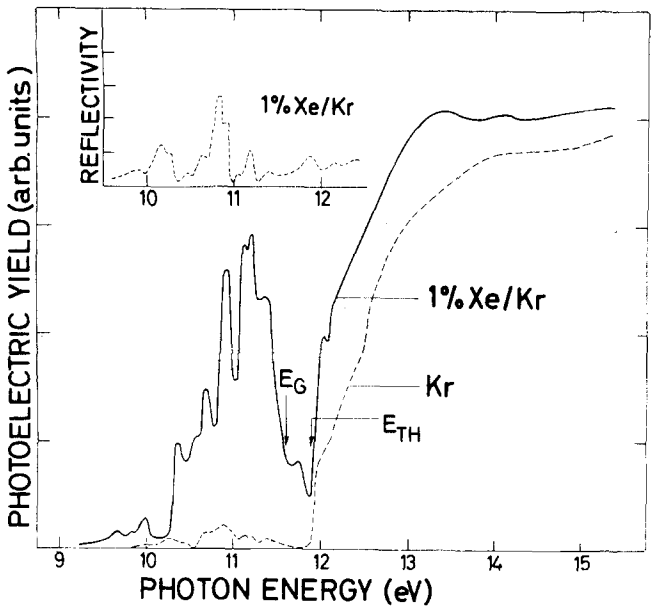

FIG. 3. Photoelectric yield per photon penetrating into the sample for 1% Xe in Kr (solid curve) and pure Kr [dashed curve (Ref. 4(a)]. The insert shows the reflectance measured simultaneously for the same sample.

clearly. Thus a higher apparent onset was assigned. An apparent higher onset has been repeated with the synchrotron radiation source when thin films of Xe/Kr were used.

The photoemission onset for Xe/Kr occurs at $E^i_{TH} = 10.3$ eV, which together with the spectroscopic value $E^i_g = 10.1$ eV, as derived from the data of Ref. 22, results in $V_0 = -0.2 \pm 0.1$ eV. Below 10.25 eV a weak photoemission yield is exhibited which cannot be assigned to an intrinsic process, as it occurs below E^i_{TH}. Electronic energy migration from the Xe impurity state to the gold substrate followed by electron ejection from the cathode may be responsible for this process.

The most remarkable difference between the photoemission spectra of Xe/Kr and of pure Kr involves the strong enhancement of the yield below E_{TH} of solid Kr, as is evident from Fig. 3. The photoemission yield between 10.3 eV and $E^{Kr}_{TH} = 11.9$ eV reaches the value of ~40%, which exceeds that of pure Kr by more than one order of magnitude. This photoemission occurs in the energy range where the Kr matrix is strongly absorbing, as is evident from Fig. 4. As in this system the maximum of the first Wannier exciton of Kr is located at 10.17 eV while $E^i_{TH} = 10.3$ eV for the Xe impurity we assert that photoemission in the range 10.3–11.9 eV originates from exciton induced photoionization of the Xe impurity. It is important to notice that light absorption into the $n = 1(\frac{3}{2})$ exciton state of Kr which peaks at 10.17 eV does not result in impurity emission, while the $n = 1(\frac{1}{2})$ state is active in exciton enhanced photoemission. This result was interpreted by asserting that the nonradiative multiphonon relaxation $n = 1(\frac{1}{2}) \rightarrow n = 1(\frac{3}{2})$ is slow on the time scale of energy transfer from "mobile" free exciton state to the impurity.

We note that the absorption maxima of the $n = 1(\frac{1}{2})$ and $n = 2(\frac{3}{2})$ exciton correspond to minima in the yield spectra (Figs. 3 and 4). A very similar behavior of the yield line shape has been observed for the Xe/Ar and C_6H_6/Xe. It will be discussed in detail for the case Xe/Ar below.

3.1.2. *Benzene in krypton*

The photoemission yield spectrum of benzene doped solid krypton (doping level ~1%) is presented in Fig. 5. We also display an extrapolation of the square root of the yield $Y^{1/2}$ as a function of energy which results in $E^{C_6H_6/Kr}_{TH} = (8.4 \pm 0.05)$ eV in agreement with the value observed previously.[23] The energy band gap $E^i_g = (8.18 \pm 0.05)$ eV of this system was determined spectroscopically.[24] These two values result in the electron affinity of solid krypton: $V_0 = E^i_g - E^i_{TH} = -(0.22 \pm 0.10)$ eV. The electron affinity obtained here compares very well with that obtained from photoemission yield measurements performed upon the pure Kr.[4a] It is also in good agreement with the experimental value observed for Xe in Kr (see above), and compares fairly with the value of -0.62 eV deduced from solely spectroscopic data where an estimate of the medium polarization by the positive hole has to be incorporated into the computation.[24] The low photoemission threshold $E^i_{TH} = 8.4$ eV $< E_1$ implies that photoemission in the range 8.4–10 eV originates from direct photoionization of the impurity.

3.2 Impurity states in argon

3.2.1 *Krypton in argon*

In Fig. 6 we display a photoelectric yield curve for a thin Ar film doped with 1% Kr. The yield from pure Ar and the simultaneously determined reflectance spectrum are given for comparison.

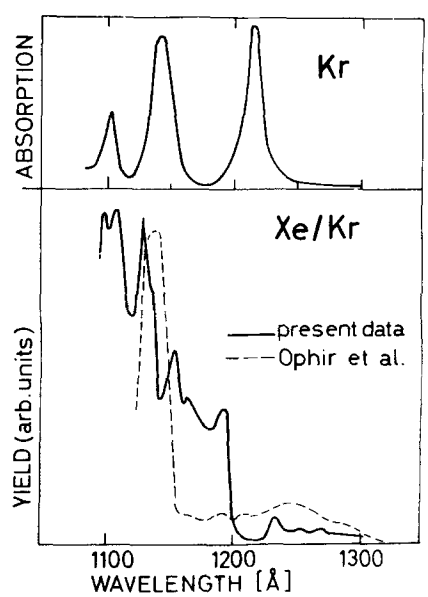

FIG. 4. Comparison of the photoelectric yield spectrum of Xe doped Kr films as observed in the present study (solid curve) and from Ref. 6 (dashed curve). The absorption of pure Kr is shown for comparison (Ref. 20).

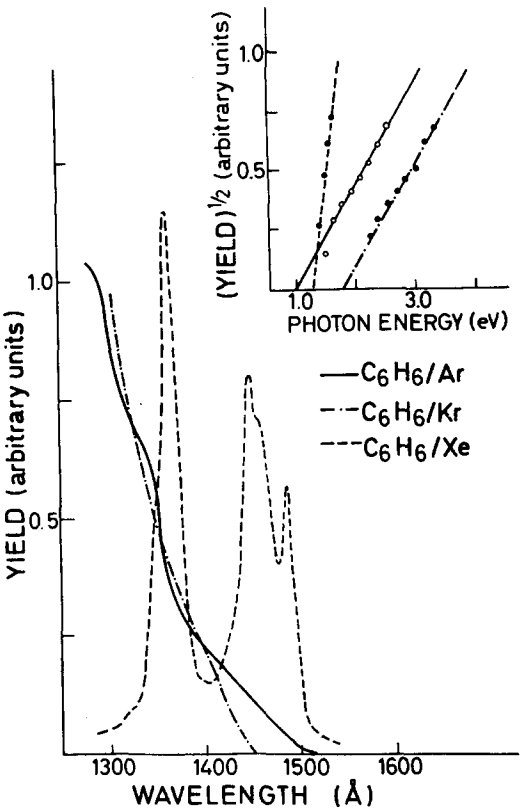

FIG. 5. Photoelectric yield spectra of solid Ar, Kr, and Xe doped with benzene. The insert shows a square root extrapolation of the yield curves.

The threshold energy for pure Ar, $E_{TH} = 13.9$ eV, and the band gap energy as obtained from the convergence of exciton series $E_g = 14.2$ eV are indicated by arrows. They result in a positive electron affinity $V_0 = +0.3$ eV.[4a] The onset in Kr/Ar is at 12.2 eV and thus the Kr impurity gap is estimated to be $E_g^i = 12.5$ eV. Compared to the pure Ar the doped films exhibit an enhanced yield between 12.2 eV and $E_{TH} = 13.9$ eV. The photoemission yield in the range 12.2–13.4 eV overlaps the host exciton series and is assigned to exciton induced impurity photoemission.

As is the case of Xe/Kr, the Kr/Ar system does not exhibit exciton induced photoemission following excitation into the $n = 1(\frac{3}{2})$ state (peaking at 12.1 eV) which is lower than E_{TH}^i, while the $n = 1(\frac{1}{2})$ is active in the energy transfer process. Again, the $n = 1(\frac{1}{2}) \rightarrow n = 1(\frac{3}{2})$ nonradiative relaxation process is slow (at the concentration employed by us) on the time scale of the energy transfer to the impurity. Finally, we notice that the exciton induced yields are larger for the higher members ($n > 1$) of the $\Gamma(\frac{1}{2})$ Ar exciton series than for the $n = 1(\frac{1}{2})$ exciton. This effect indicates that electronic relaxation between the high members of the $\Gamma(\frac{1}{2})$ exciton series and the $n = 1$ exciton level is not "instantaneous" on the time scale of electronic energy transfer. In this way excitation into different n states of the host Wannier series will, after energy transfer to the impurity, result in electrons originating from the same impurity level but with different kinetic energies. The energy dependence of the escape length will modify the yields at different energies. More interesting, the impurity photoionization cross sections and the exciton diffusion length can depend on the n state. These problems deserve further study.

3.2.2. *Benzene in argon*

As shown in Fig. 5 the photoemission threshold of benzene doped solid argon is observed at an energy of $E_{TH}^{C_6H_6/Ar} = (8.0 \pm 0.05)$ eV, in agreement with the value observed previously.[23] The energy band gap obtained from absorption spectroscopy is $E_g^{C_6H_6/Ar} = (8.51 \pm 0.05)$ eV,[24] resulting in $V_0 = (+0.5 \pm 0.1)$ eV. The system of C_6H_6 in Ar provides an example for direct impurity photoionization.

3.2.3. *Xenon in argon*

The photoelectric yield curve for pure Ar and for a sample containing 0.3% Xe are compared in Fig. 7. The threshold energy $E_{TH} = 13.9$ eV and band gap $E_g = 14.2$ eV of the host are marked by arrows. A more detailed spectrum near the onset of the Xe impurity (Fig. 8) results in $E_{TH}^i = 10.2$ eV whereupon from $E_G^i = 10.54$ we get $V_0 = +0.34$ eV for solid Ar.

In the energy region below $E_{TH} = 13.9$ eV two distinct photoemission mechanisms are exhibited in Xe/Ar. In the range 10.2–11.9 eV below the $n = 1(\frac{3}{2})$ exciton of Ar, emission originates from direct photoionization of the impurity. In the range 11.9–13.9 eV exciton induced photoemission is exhibited while above 13.9 eV intrinsic photoemission from the host matrix takes place. The photoemission line shapes for different film thickness d are displayed in Fig. 9. Figure 10 portrays photoemission in the energy range 11–15 eV, where induced exciton photoionization takes place together with the ab-

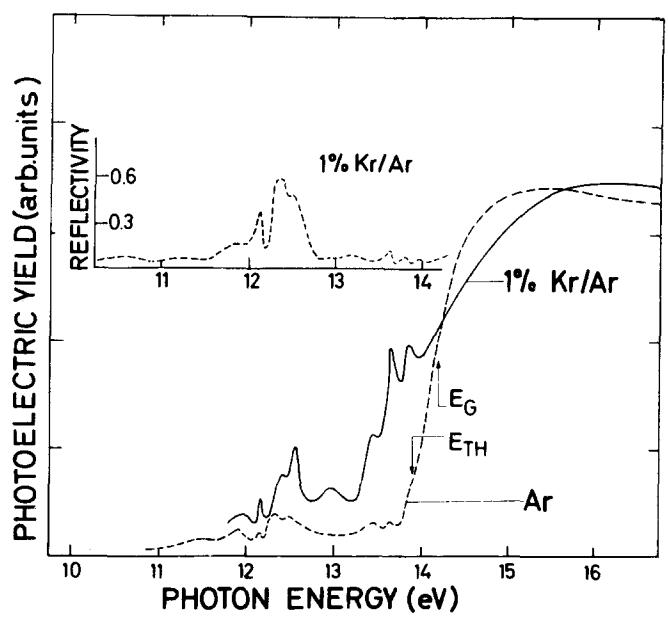

FIG. 6. Photoelectric yield per photon penetrating into the sample for 1% Kr in Ar (solid curve) and pure Ar [dashed curve (Ref. 4(b)]. The insert shows the reflectance measured simultaneously.

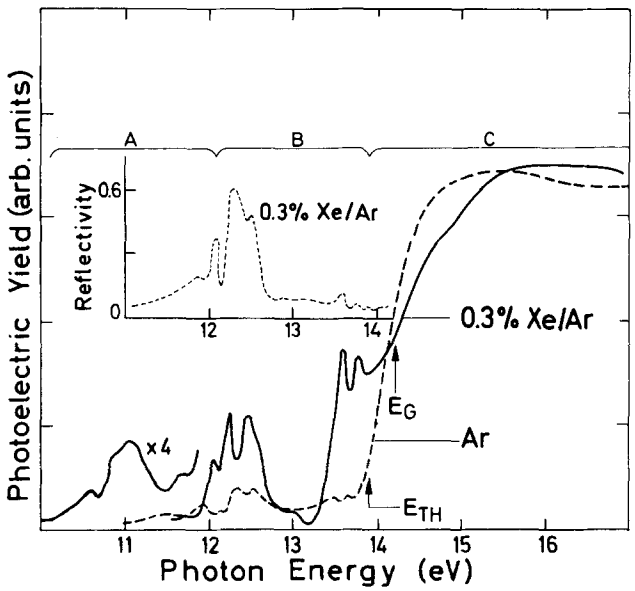

FIG. 7. Photoelectric yield per photon penetrating into the sample for 0.3% Xe in Ar (solid curve) and pure Ar [dashed curve (Ref. 4(b)]. The insert shows the reflectance measured simultaneously. The three photoemission ranges A, B, and C are indicated (see text).

sorption spectrum of solid Ar as obtained from an analysis of the optical constants.[19] These photoemission yield curves exhibit some interesting features.

(a) At high d values Y exhibits minima at 12.1, 12.25, and 13.6 eV. These minima correspond to the maxima of the $n=1(\frac{3}{2})$, $n=1(\frac{1}{2})$, and $n=2(\frac{3}{2})$ Ar exciton states, respectively.

(b) The $n=2(\frac{1}{2})$ exciton state coincides with a maximum of the Y curve exhibited at all d values.

(c) Decreasing the film thickness from 800 to 370 Å results in the disappearance of the minimum in the Y curve at 13.6 eV which is replaced by a maximum coinciding with the $n=2(\frac{3}{2})$ exciton peak.

(d) For even thinner films, $d \sim 90$ Å, the minima at 12.1 and 12.25 eV are replaced by maxima which coincide with the $n=1(\frac{3}{2})$ and $n=1(\frac{1}{2})$ exciton states, respectively.

We note in passing that the d dependence of the Y curve for doped solid rare gases differs drastically from the behavior of pure rare gas solids where Y below E_{TH} is independent of the thickness.[4b] These features provide important information concerning exciton dynamics in this system and will be analyzed in Sec. 4.2.

Another interesting feature of these results should be mentioned. Further in the high energy part of the spectrum at 19 eV the decrease of the relative photoelectric yield (as compared to Y at photon energies $\hbar\omega < \sim 17$ eV) is more pronounced for the thicker films. An example is shown in Fig. 11 for the dependence of the photoyield on the xenon concentration.

3.3 Electron escape length in pure solid Ar

An attempt was made to measure the escape length L of electrons in pure solid Ar by monitoring the photo-

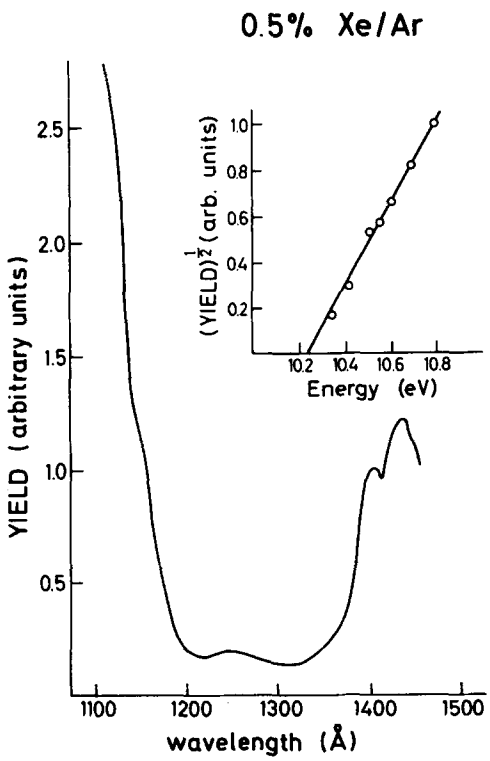

FIG. 8. Photoelectric yield for 0.5% Xe in Ar in the threshold region. The insert shows a square root extrapolation of the yield.

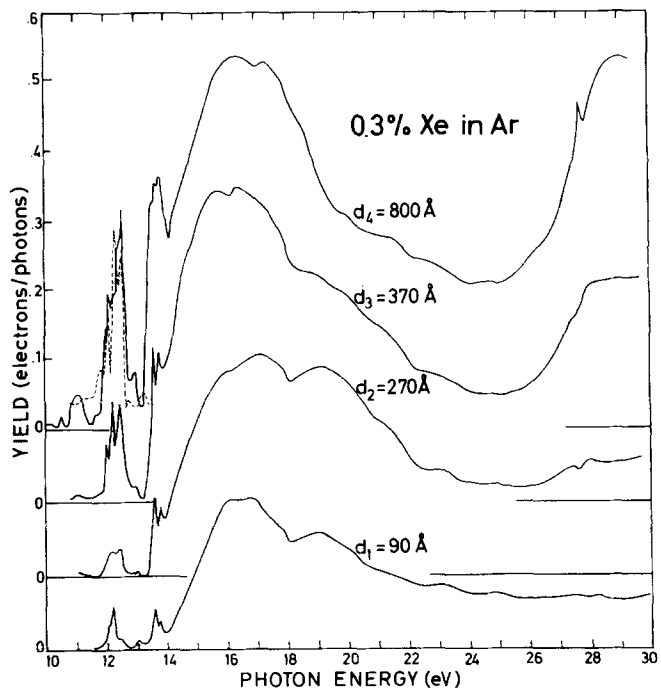

FIG. 9. Photoelectric yield per photon penetrating into the sample for 0.3% Xe in Ar for four different film thicknesses $d_1 = 90$ Å, $d_2 = 270$ Å, $d_3 = 370$ Å, and $d_4 = 800$ Å. The dashed curve is the reflectance measured for the thickest film, d_4.

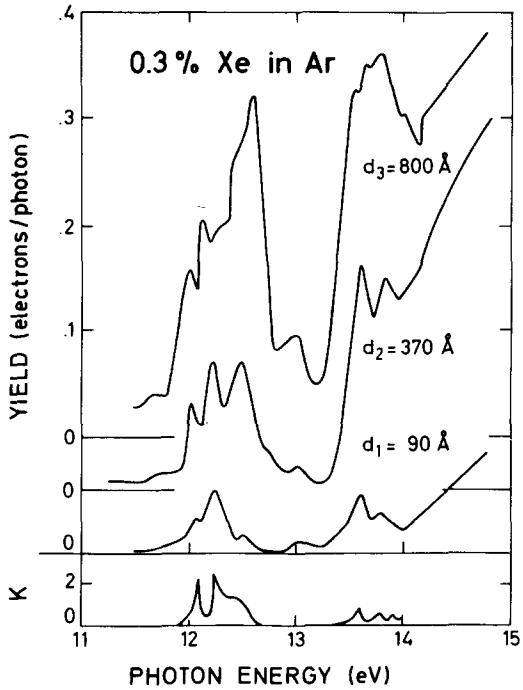

FIG. 10. Photoelectric yield per photon penetrating into the sample for 0.3% Xe in Ar in the excitonic range for three different film thicknesses. The absorption coefficient k ($\tilde{n} = n + ik$) of pure Ar is given for comparison (Ref. 19).

current from the gold emitter electrode as a function of the thickness of pure Ar. We present here preliminary results. Further work is in progress. The excitation of the gold substrate was conducted in the energy range 8–10 eV where solid argon is optically transparent. The films were deposited at the rate of 90 Å/min, the thickness being determined by oscillation in the transmittance of visible light at 6600 Å. We expect the photocurrent to be given by $i = i_0 \exp(-d/L)$. The result for several photon energies are presented in Fig. 12. They exhibit two components. The short component is characterized by $d = 220$ Å and is tentatively assigned to primary surface coverage layer which exhibits strong efficient energy loss effects. For thicker samples ($d > 200$ Å) we get $L = 1350$ Å at 8.00 eV, $L = 1250$ Å at 8.70 eV, and $L = 1950$ Å at 9.18 eV.

4. DISCUSSION

Following the basic classification of the photoemission mechanisms in lightly doped solid rare gases which were presented in Sec. I, it is convenient to divide the photoelectric yield curves into three different spectral region, which we shall name A to C in order of increasing photon energy. In region A direct photoionization of the guest impurities above the vacuum level is observed. In region B, the spectral range where the exciton band of the host matrix is located, exciton induced impurity ionization occurs. Finally, in region C, located above E_{TH} for the host, direct photoemission from the host matrix is exhibited.

In Table I we have identified these three regions for the systems studied in the present work. The following general features of these three regions should be con-

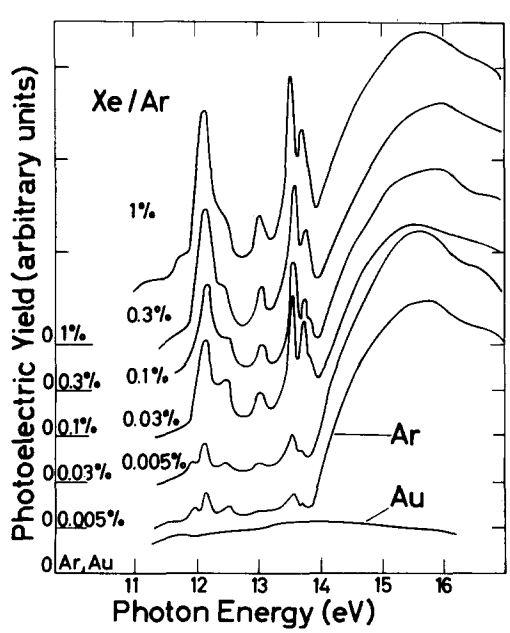

FIG. 11. Dependence of the photoelectric yield of Xe doped Ar films on the Xe concentration. The film thickness is 60 Å. The spectra are not corrected for the hot electron contribution from the gold substrate and the reflectivity. Photoelectric yield curves for the gold substrate and for pure Ar films are also shown.

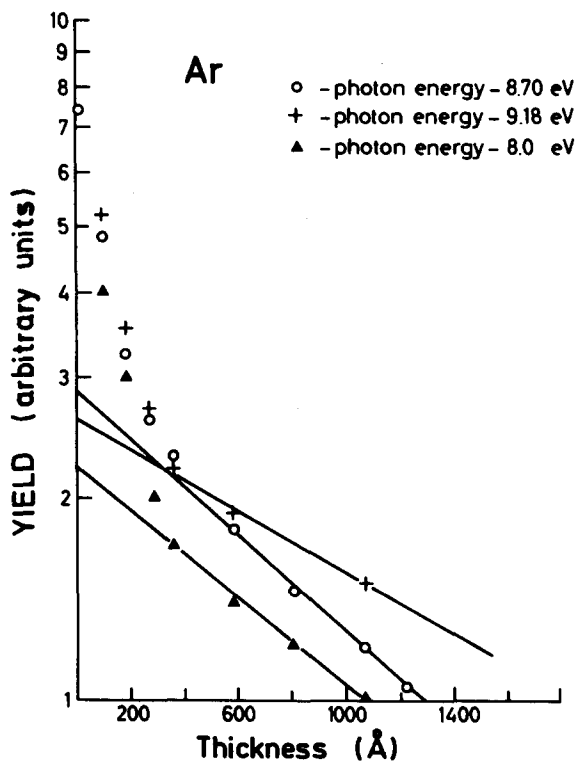

FIG. 12. Dependence of the photocurrent of hot electrons from the gold substrate on the thickness of pure Ar overlayer for three different photon energies $\hbar\omega_1 = 8.0$ eV, $\hbar\omega_2 = 8.70$ eV, and $\hbar\omega_3 = 9.18$ eV. For these energies the Ar films are transparent.

TABLE I. Segregation of photoemission ranges in doped solid rare gases (energies in eV). Blanks have not been measured.

	A	B	C
Xe/Kr	not existing	10.3–11.9	>11.9
Xe/Ar	10.8–11.9	11.9–13.9	>13.9
Kr/Ar	not existing	11.9–13.9	>13.9
C_6H_6/Ar	8.00–11.9		
C_6H_6/Kr	8.40–10.1		
C_6H_6/Xe	not existing	8.15–9.7	>9.7

sidered.

(1) In *region A* the line shape of the Y curve when properly corrected for the substrate photoemission is independent of the thickness and of impurity concentration. The situation is reminescent of photoemission from the pure solids.

(2) In *region B* the Y curve exhibits a marked dependence on the film thickness and of the impurity concentration.

(3) In *region C* the general appearance of the yield curve is not very sensitive to the sample thickness and the impurity concentration. However, at higher energies, above ~17 eV, such effects, which are not well understood, were exhibited in the Xe/Ar system.

We now proceed to extract further information from these data regarding energy levels and exciton dynamics.

4.1 Electron affinities

Pedestrian but relevant information from our data involves the threshold energies for photoemission from impurity states. The E^i_{TH} values are, of course, independent of whether direct impurity photoionization or energy transfer induced impurity photoionization takes place. A comment concerning the accuracy of the E^i_{TH} data is in order. There is at present no rigorous justification for a particular functional form for an extrapolation of the yield curves for insulators near threshold. Simple square root extrapolations are reasonable.[25] Figure 13 provides a comprehensive view of the threshold regions for the various systems that were studied by us and extrapolated this way. The V_0 values obtained from the present study combining the photoemission E^i_{TH} and the spectroscopic E^i_g data are summarized in Table II together with the data for the pure solids. The satisfactory agreement obtained for the V_0 values for the impurity states and the pure solids provides additional strong support for the assignment of the Wannier impurity states in the doped rare gases.

A comparison of the V_0 values for solid Ar ($V_0 = +0.3$) with the available experimental $V_0 = -0.33$ eV[7d] and theoretical $V_0 = -0.45$ eV for liquid Ar[26] indicates that in the solid the relative importance of the short range repulsive kinetic energy contribution is somewhat larger than in the liquid, thus correcting an earlier theoretical estimate.[24] Another kind of useful energetic information which can be extracted from the experimental impurity photoemission thresholds involves the polarization energy P_+ of the medium by the positive impurity ion. Utilizing Eqs. (1.1) and (2.2) we readily have

$$P^i_+ = E^i_{TH} - I^i_g,$$

and these data are assembled in Table III. The resulting polarization energies are reasonable and can be accounted

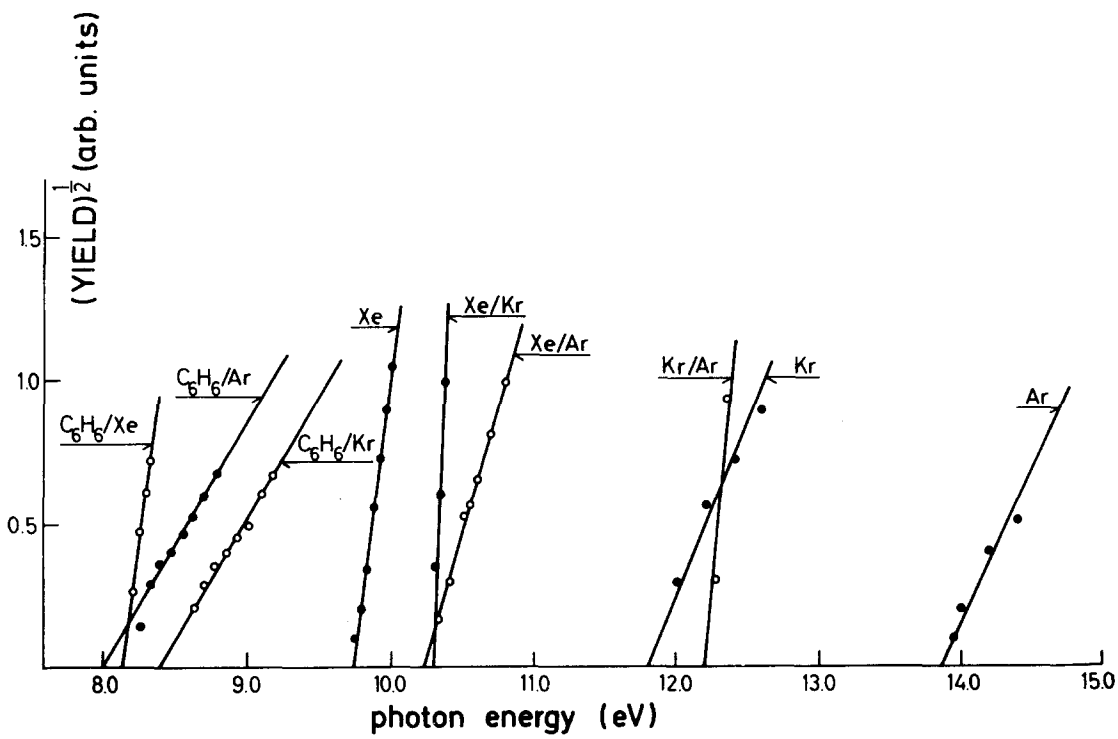

FIG. 13. Onset of strong photoelectron emission for pure rare gases (Ref. 4a) and various guest-host matrix combinations.

TABLE II. Energy gap E_g threshold energy E_{TH} and V_0 values ($V_0 \equiv -E_A$) for pure and doped rare gases (energies in eV).

System	E_g or E_g^i	E_{TH} or E_{TH}^i	$V_0(\equiv -E_A)$	Matrix
Ne (pure)[a]	21.4	21.4 ± 0.1	0.0 ± 0.1	Ne
Reference e		20.2 ± 0.2	1.2 ± 0.2	
Ar (pure)[b]	14.2	13.9	0.3	Ar
Kr in Ar[c]	12.5	12.2	0.3	Ar
Xe in Ar[c]	10.54	10.23	0.31	Ar
C_6H_6 in Ar[c]	8.51	8.00	0.51	Ar
Kr (pure)[b]	11.6	11.9	−0.3	Kr
Xe in Kr[c]	10.1	10.30	−0.2	Kr
C_6H_6 in Kr[c]	8.18	8.4	−0.22	Kr
Xe (pure)[b]	9.3	9.7	−0.4	Xe
Reference d	9.28	9.74	−0.46	
C_6H_6 in Xe[c]	7.75	8.15	−0.4	Xe

[a]Reference 4c. The experimental value for V_0 constitutes a lower limit for V_0 and does not exclude the possibility that V_0 is positive.
[b]Reference 4a.
[c]This work.
[d]Reference 6.
[e]Results from energy distribution measurements, Ref. 35.

for in terms of refined semiclassical calculations. A first step in that direction was already attempted.[27]

After establishing a reliable set of V_0 values, we are convinced that the E_{TH}^i data and, with some minor numerical corrections, the energy level scheme for atomic[22] and molecular[24] Wannier impurity states are self-consistent and reliable. On the strength of this evidence we can proceed to consider the problem of exciton dynamics.

4.2 Exciton induced photoemission

Impurity ionization originating from electronic energy transfer from an exciton state bears a close analogy to Penning ionization[28] in the gas phase and to exciton collisions resulting in Auger-type ionization in organic crystals. The present study demonstrated the generality of exciton induced impurity photoionization process in solid rare gases. We shall first consider the energetics of this process. The E_{TH}^i values together with the available data on the optical luminescence spectra of homonuclear rare gas diatomic molecules in these solids[10,29] (see Table IV) conclusively rule out the possibility of electronic energy transfer from the trapped exciton (i.e. the diatomic molecule) to the impurity states studied by us. It is also evident from the data assembled in Table IV that this process can occur from

TABLE III. P_+ values for atomic and molecular impurities (energies in eV).

Host	Guest	E_{TH}^i	I_g^i	P_+^i
Ar	Kr^+	12.2	14.0	−1.8
Ar	Xe^+	10.2	12.13	−1.93
Kr	Xe^+	10.3	12.13	−1.83
Ar	$C_6H_6^+$	8.0	9.24	−1.24
Kr	$C_6H_6^+$	8.4	9.24	−0.84
Xe	$C_6H_6^+$	8.15	9.24	−1.09

TABLE IV. Activity of the lowest $n=1(\frac{3}{2})$ exciton in impurity induced ionization (energies in eV).

System	$E_1^{(3/2)}$[a]	E_{TH}^i	$E_1^{(3/2)}$ active	$E_M \pm \Delta$[b,c]
Xe/Ar	12.1 (0.3)	10.2	+	9.93 ± 0.53
Xe/Kr	10.17 (0.15)	10.3	−	8.35 ± 0.39
Kr/Ar	12.1 (0.3)	12.2	−	9.93 ± 0.53
C_6H_6/Xe	8.36 (0.16)	8.15	+	7.10 ± 0.30

[a]Numbers in brackets represent the linewidth (Ref. 24).
[b]E_M, peak energy of molecular emission of diatomic molecules in solids (Ref. 10a).
[c]Δ, linewidth in molecular emission (Ref. 10a).

the lowest lying $n=1(\frac{3}{2})$ exciton for impurity states characterized by a moderately low value of E_{TH}^i, or from higher exciton states when $E_1 < E_{TH}^i$. We thus conclude that in general exciton states play the role of energy donors in this process.

After having established the nature of the energy donor states in our system the next question pertains to the problem of the mechanism of the energy transfer process. Most interesting in this context is the question whether the process can be described in terms of long range dipole interactions between a static excitation or whether exciton motion has to be invoked for the proper interpretation of the data. The simplest kinetic scheme involving competition between exciton trapping and energy transfer from immobile excitons to homogenously distributed impurities is governed by the equation

$$\frac{\partial n(x,t)}{\partial t} = \alpha I_0 e^{-\alpha x} - \frac{n(x,t)}{\tau_0} - S[R]\, n(x,t), \tag{4.1}$$

where $n(x,t)$ is the number density of "free" excitons at the distance x from the surface, α the absorption coefficient, I_0 the incident light intensity, S is the rate constant for impurity ionization, $[R]$ the impurity concentration, and τ_0 the free exciton lifetime. Under steady state conditions $n(x,t) = n(x)$ and we get

$$n(x) = \alpha \tau I_0 e^{-\alpha x}. \tag{4.2}$$

The photoemission yield is now

$$Y = \frac{S[R]}{I_0} \int_0^d e^{-x/L}\, n(x)\, dx, \tag{4.3}$$

whereupon Eqs. (2) and (3) result in

$$Y = \tau S(R) \frac{\alpha L}{\alpha L + 1} \left\{ 1 - \exp\left[-\frac{d}{L} (\alpha L + 1) \right] \right\}, \tag{4.4}$$

where

$$\tau = (1/\tau_0 + S[R])^{-1}. \tag{4.5}$$

Equation (4.4) does not provide a proper interpretation for the energy dependence and the d dependence of Y for Xe/Ar mixtures which was presented in Sec. 3.2. In particular, this simple approach cannot explain the dips in the photoemission curves for thick samples which coincide with the exciton absorption peaks.

TABLE V. Exciton lifetimes and exciton diffusion length in molecular crystals.

Crystal	Exciton	τ_0(sec)	l_0 (Å)	Reference
Anthracene	singlet	25×10^{-9}	150	a
Anthracene	triplet	25×10^{-3}	10^5	b
Xe	$n=1(\frac{3}{2})$	$\sim10^{-12}$–10^{-11}	75	c
Ar	$n=1(\frac{3}{2})$	10^{-12}–10^{-11}	120	Present work

[a]O. H. Simpson, Proc. Roy. Soc. A **238**, 402 (1957).
[b]M. Levine, A. Szoke, and J. Jortner, J. Chem. Phys. **45**, 1591 (1966).
[c]Reference 6.

We conclude that a physical model involving immobile excitons cannot provide an adequate interpretation of the experimental data and are inevitably led to a physical picture which involves energy transfer from mobile excitons competing the exciton trapping. Equation (4.1) is now generalized to incorporate exciton diffusion whereupon the number density $n(x, t)$ of free mobile excitons is governed by the diffusion equation

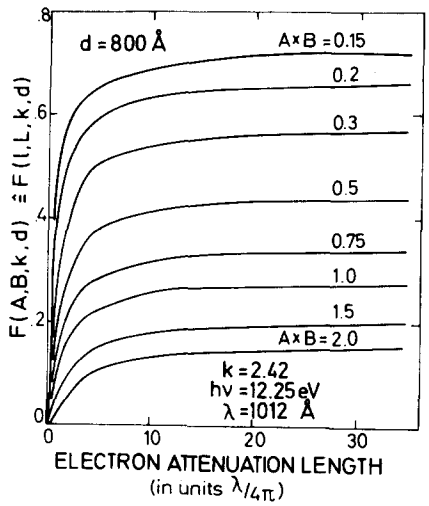

FIG. 15. Calculated diffusion and escape term $F(l, L, k, d)$ of the photoelectric yield as a function of the electron attenuation length A (in units $\lambda/4\pi$). The exciton diffusion length l (in units $\lambda/4\pi$) is taken as a parameter.

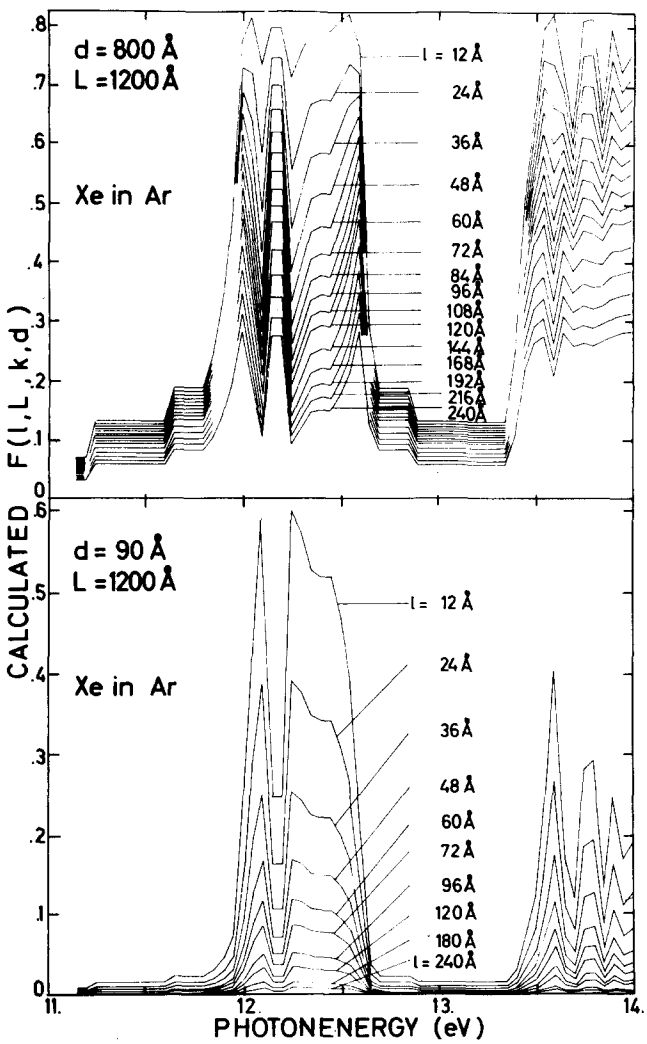

FIG. 14. Calculated photoemission yield spectra for Xe doped Ar films for film thicknesses $d=90$ Å and $d=800$ Å. The electron escape length L is taken to be 1200 Å, the excition diffusion length l is varied between 12 and 240 Å.

$$\frac{\partial n(x,t)}{\partial t} = D\frac{\partial^2 n(x,t)}{\partial x^2} + \alpha I_0 e^{-\alpha x} - \frac{n(x,t)}{\tau_0} - S[R]\,n(x,t), \quad (4.6)$$

where D is the exciton diffusion coefficient. Under steady state conditions the solution is

$$n(x) = \frac{\alpha\tau I_0}{\alpha^2 l^2 - 1}\left(Ae^{-x/l} + Be^{x/l} - e^{-\alpha x}\right), \quad (4.7)$$

where the effective exciton lifetime is given by Eq. (4.5) and the (concentration dependent) exciton diffusion length in the doped crystal is

$$l = \{D(1/\tau_0 + S[R])^{-1}\}^{1/2}, \quad (4.8)$$

being related to the diffusion length in the pure crystal

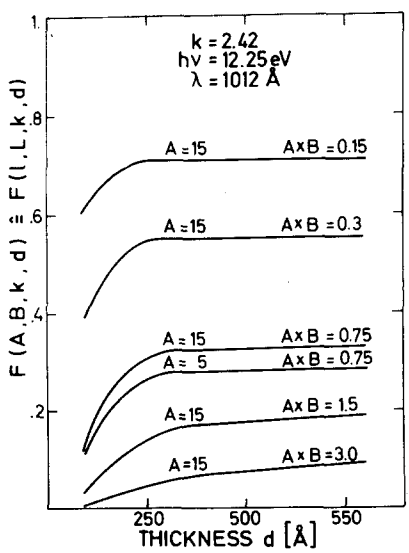

FIG. 16. Calculated diffusion and escape term $F(l, L, k, d)$ of the photoelectric yield as a function of the film thickness d. The exciton diffusion length l (in units $\lambda/4\pi$) is taken as a parameter.

$$l_0 = (D\tau_0)^{1/2} \tag{4.9}$$

via

$$l = l_0(1 + S\tau_0[R])^{-1/2}. \tag{4.10}$$

The boundary conditions appropriate for a film of finite thickness are

$$n(0) = 0, \quad n(d) = 0, \tag{4.11}$$

which result in the following expression for A and B:

$$A = \frac{\exp(-\alpha d) - \exp(d/l)}{\exp(-d/l) - \exp(d/l)}, \tag{4.12}$$

$$B = \frac{\exp(-d/l) - \exp(-\alpha d)}{\exp(-d/l) - \exp(d/l)}. \tag{4.13}$$

The photoemission yield (4.3) takes the form

$$Y = \frac{S[R]\tau\alpha}{\alpha^2 l^2 - 1}\left\{\frac{ALl}{L+l}\left[1 - \exp\left(-\frac{d}{l} - \frac{d}{L}\right)\right] + \frac{BLl}{l-L}\left[1 - \exp\left(\frac{d}{l} - \frac{d}{L}\right)\right] - \frac{L}{\alpha L + 1}\left[1 - \exp\left(-\alpha d - \frac{d}{L}\right)\right]\right\}. \tag{4.14}$$

We note in passing that in the limit $l \to 0$ (i.e. $l_0 \to 0$ or large values of $S\tau_0[R]$) $Y \propto \alpha L(\alpha L + 1)^{-1}$ for thick samples, exhibiting a monotonous increase of Y with α. Our observation of a minimum in the Y curve at the maxima of the $n = 1(\frac{3}{2})$, $n = 1(\frac{1}{2})$ and $n = 2(\frac{3}{2})$ excitons of Ar implies that l is finite and that exciton diffusion occurs. The experimental data for the thickness and concentration dependence of the Y curves in Xe/Ar mixtures were analyzed according to Eqs. (4.8)–(4.14) together with (4.5) invoking the following simplifying assumptions.

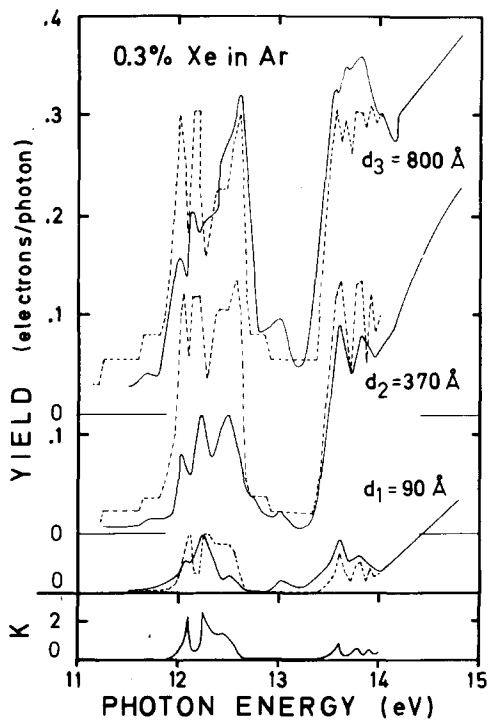

FIG. 17. Comparison of calculated and measured photoelectric yield curves for 0.3% Xe in Ar for three film thicknesses. For the calculation $l = 60$ Å, $L = 1200$ Å and $S\tau[\mathrm{Xe}] = 1$ as well as the absorption coefficient shown have been used.

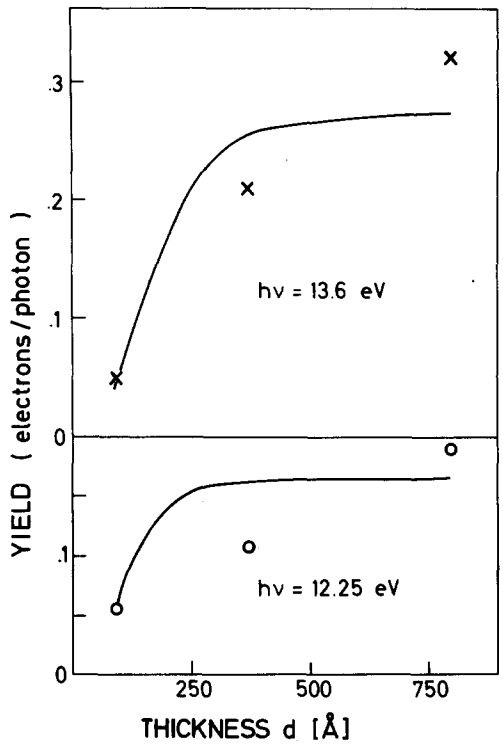

FIG. 18. Absolute photoelectric yield as a function of film thickness d. The solid curves give the calculated yield using $A = 15$, $B = 0.05$. Crosses and circles give the experimental results.

(a) The exciton diffusion length l at a given impurity concentration is constant for all excitation energies. This assumption can be justified provided that the rate of multiphonon radiationless relaxation[30] of higher (n

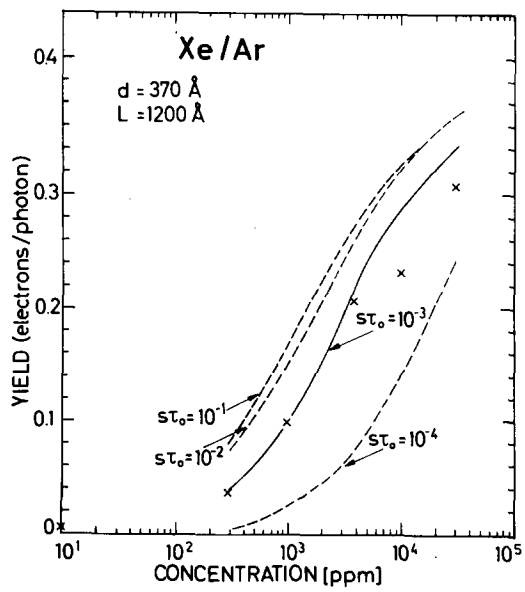

FIG. 19. Measured and calculated concentration dependence of the yield for Xe/Ar mixtures using a film thickness of 370 Å. The yield was calculated for different parameters $S\tau_0$ (dashed lines). The solid curve shows the best fit for $S\tau = 10^{-3}$ (ppm^{-1}). The electron attenuation length was taken as 1200 Å.

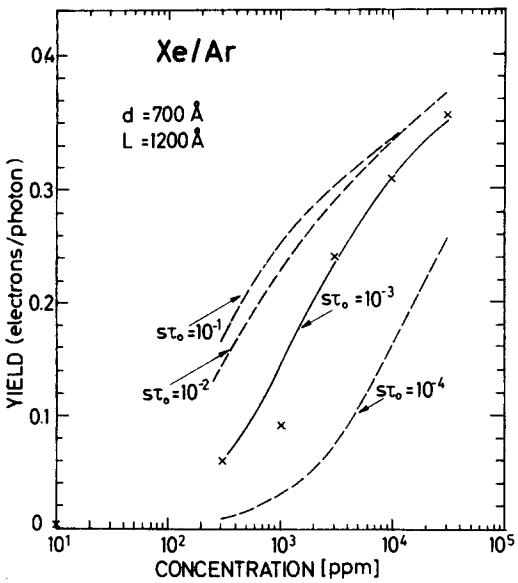

FIG. 20. The same as Fig. 19 but for a film thickness of d =700 Å. Again the value of $S\tau_0=10^{-3}$ (ppm^{-1}) fits the measurement.

>1) exciton states to the lowest $n=1(\frac{3}{2})$ and $n=1(\frac{1}{2})$ exciton states is fast on the time scale of the effective exciton lifetime τ. All the energy transfer process will then occur from the $n=1$ exciton states, and the diffusion lengths of the $n=1(\frac{3}{2})$ and $n=1(\frac{1}{2})$ excitons are expected to be similar. A rigorous justification for this assumption would be possible, if in addition to the conditions stated above the $n=1(\frac{1}{2})\rightarrow n=1(\frac{3}{2})$ radiationless relaxation is ultrafast. However, this latter condition does not hold for Xe/Ar and Kr/Ar systems (see Secs. 3.1 and 3.2). In view of our ignorance regarding rates of nonradiative relaxation of high exciton states we shall refrain from advancing more complex kinetic schemes involving several exciton states and adopt this simplifying assumption concerning the energy independence of l. We should bear in mind that more detailed and accurate experiments of the type described herein might provide pertinent information concerning the radiationless relaxation rates between high and low Wannier exciton states.

(b) We assume that the electron escape length L is weakly varying with the excitation energy. We have demonstrated in Sec. 3.3 that L is practically constant within the margin of experimental error in the energy range 8–10 eV, and we shall take $L\simeq 1200$ Å also for the higher 11–14 eV region. Provided that the electronic relaxation rate between exciton states is fast relative to τ^{-1} this assumption is fully satisfied.

(c) Energy transfer cross sections resulting in the formation of $Xe^+(^2P_{3/2})$ dominates over the low 11–11.5 eV energy range, where we have neglected the possibility of formation of $Xe^+(^2P_{1/2})$, a process which will not result in photoemission. This result is an overestimate of the calculated photoemission yield at these "low" energies. At higher energies above 11.5 eV we assume that both levels $Xe^+(^2P_{3/2})$ and $Xe^+(^2P_{1/2})$ contribute via energy transfer.

Under these circumstances, Eq. (4.14) is rewritten in the form

$$Y(E)=S\tau[R]\,F(l(R),L,k(E),d), \tag{4.15}$$

with k being the absorption coefficient $[\tilde{n}=(n+ik)]$, where we have separated a kinetic type contribution $S\tau[R]$ from the diffusion and escape term F.

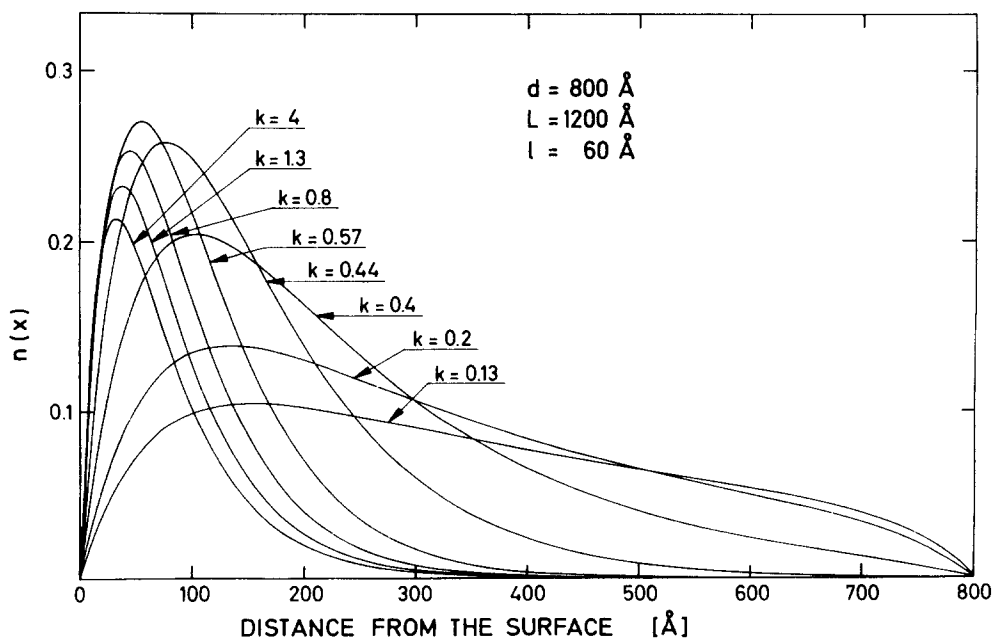

FIG. 21. Calculated number of free mobile excitons $n(x)$ at distance x from the surface for 800 Å thick film using the diffusion model for different absorption coefficients k. An exciton diffusion length of $l=60$ Å and an electron attenuation length $L=1200$ Å are used.

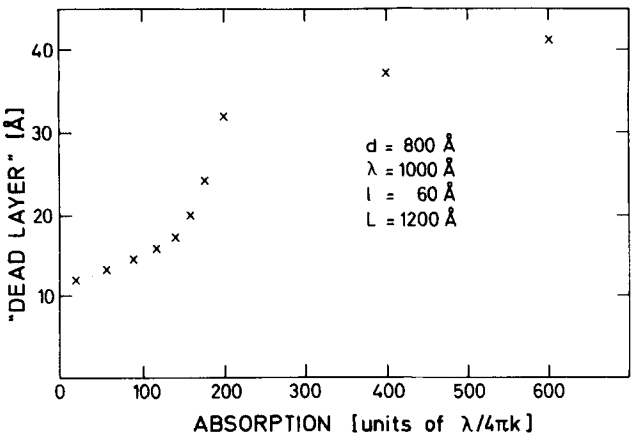

FIG. 22. Dependence of the inherent "dead layer" of the diffusion model on the absorption coefficient. As dead layer the distance corresponding to $(1-e^{-1})$ of the maximum value of $n(x)$ was taken from Fig. 21.

At constant d and $[R]$ the photoemission yield is determined by three parameters:

$$A=(4\pi/\lambda)L, \quad B=l/L, \quad C=S\tau, \tag{4.16}$$

where λ is the light wavelength. At high Xe concentration we expect that $C[\mathrm{Xe}]\to 1$ and $Y=F$ being determined by A and B only. Numerical calculations of Y vs E at such high concentrations were performed utilizing the experimental absorption coefficients[19] of solid Ar over a wide range of A and B parameters. Representative data for two film thicknesses $d=800$ Å and $d=90$ Å are presented in Fig. 14. From these numerical results we assert that for thick films the symmetric splitting of the Y curve around $n=1(\frac{3}{2})$, $n=1(\frac{1}{2})$ and $n=2(\frac{3}{2})$ exciton states occurs for a large number of A and B pairs for which $A>10$ ($L>800$ Å) and $B>0.03$ ($l>24$ Å). The proper A value may be chosen by the experimental determination of $L\simeq 1200$ Å at low energies which implies $A=15$. Alternatively, we can utilize absolute quantum yields for the determination of A and B which simultaneously result in the symmetric splitting and give the proper absolute Y values say at the three lowest exciton peak energies. In Fig. 15 we plot the calculated Y values at several energies as a function of A and B, noting that Y is determined by the product $A\times B$ that is by l rather than by A and B separately. The same behavior is also exhibited for thin films. Finally, the thickness dependence of Y at a given energy is plotted for different $A\times B$ $(4\pi l/\lambda)$ values in Fig. 16.

We start with high concentration $[\mathrm{Xe}]=0.3\%$, where we assume that $S\tau[\mathrm{Xe}]\simeq 1$. A semiquantitative fit of the $Y(E)$ curves at different thicknesses and the absolute values of Y was accomplished with the parameters

$$L=1200 \text{ Å}, \quad l/L=0.05,$$

the first value being consistent with the experimental L value. In Fig. 17 we compare the $Y(E)$ theoretical and experimental line shapes at different d values. The calculated curves have been divided by a factor of 2, thus taking into account that only half of the numbers of excited electrons have a momentum component towards the surface. In view of this assumption, the agreement is satisfactory. In Fig. 18 we present the absolute Y values at two energies as a function of d; again the results are gratifying. Finally, the parameter $C=S\tau_0$ was determined for the concentration dependence in the energy range spanning the $n=2$ and $n=3$ excitons of Ar for two film thickness, corresponding to $d=370$ and 700 Å. In Figs. 19 and 20 we compare the experimental concentration dependence with the predictions of the dif-

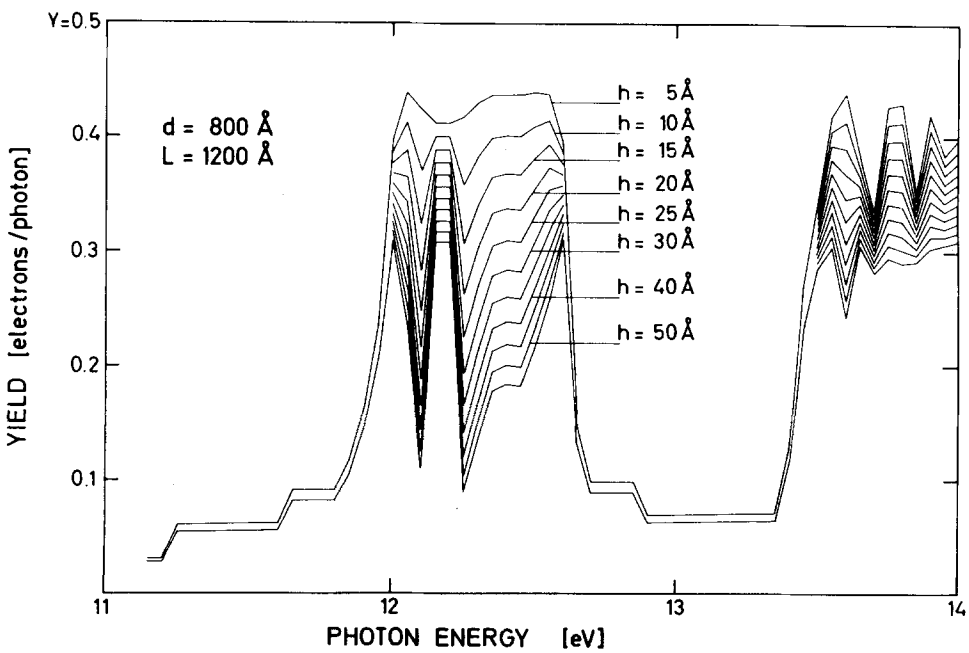

FIG. 23. Calculated spectral dependence of the yield using the dead layer model [Eq. (4.18)] for several thicknesses h of the dead layer. The same absorption coefficients as in Fig. 10 and an electron attenuation length of 1200 Å are used.

fusion model. The best fit between theory and experiment was accomplished taking $S\tau_0 = 10^{-3}$ (ppm)$^{-1}$ or $S\tau_0 = 6\times 10^{-20}$ cm^{-3} in more conventional units.

This result together with $l \simeq 60$ Å at 0.3% (Xe) yields with the aid of Eq. 4.11 the value of $l_0 = 120$ Å for the exciton diffusion length in molecular crystals. The exciton diffusion length in Ar obtained herein is close to that in Xe implying an exciton diffusion coefficient of ~ 1 cm^2 sec^{-1}. The approximate value of $S \simeq 6\times 10^{-8}$ cm^{-3} sec^{-1} for the $n=1$ exciton of the Xe impurity in Ar is not far from the value 5×10^{-7} cm^{-3} sec^{-1} for the $n=1$ exciton in solid Xe.[6] Both values were estimated taking $\tau_0 \simeq 10^{-12}$ sec. The diffusion coefficient for solid Ar can be used to extract a mean free path Λ for scattering of Wannier excitons. Setting $D = \langle V^2\rangle^{1/2}\Lambda$ where $\langle V^2\rangle^{1/2}$ is the rms exciton group velocity, $\langle V^2\rangle^{1/2} \approx Ma/\hbar$, where $M \simeq 0.1$–0.5 eV corresponds to the exciton band width and $a = 5$ Å is the internuclear spacing, we get $\Lambda \simeq \hbar D/Ma$. Thus $\Lambda \simeq 2.4$–12 Å, which is of the order of the lattice spacing and the exciton motion is diffusive, rather than coherent.

We have now to elucidate the nature of the "hidden" approximations involved in the diffusion model. These will be segregated into the nature of the exciton motion in the bulk and the cardinal role of surface effects. The diffuse motion of the free $n=1$ Wannier exciton implicitly assumed by us is self-consistent with the short mean free path deduced from the diffusion coefficient and furthermore is compatible with the large optical half linewidth (~ 0.1 eV) of the $n=1$ exciton exhibited in the optical spectra of pure rare gases.[2] The large optical linewidth which exceeds the theoretical estimate, based on Toyozawa's weak exciton–phonon coupling theory,[30] by about one order of magnitude implies strong coupling between the "free" $n=1$ exciton (prior to exciton trapping) and the lattice phonons, whereupon exciton scattering occurs at each lattice site. Thus the application of a classical diffusion equation is fully justified.

Turning now to the role played by surface and boundary effects we focus attention on the boundary conditions, Eq. (4.11), utilized by us. The condition $n(d)=0$ is fully justified as we have recently demonstrated[4b,31] that the extrinsic weak photoemission resulting from optical excitation of bound Wannier exciton states, located below E_{TH}, originates from exciton diffusion to the gold substrate followed by electronic energy transfer which results in electron ejection from the substrate. Thus the $n=1$ excitons are destroyed at $x=d$. The second boundary condition $n(0)=0$ is more subtle. For an ideal crystal extending to the lower boundary $x=0$, it might have been preferable to utilize Simpson's boundary condition[32] $D\,\partial n/\partial x = 0$ at $x=0$, which implies that the exciton flux vanishes on the outer surface. From the operational point of view this boundary condition does not provide an adequate interpretation of our experimental results. Furthermore, surface effects will probably result in enhanced exciton trapping or exciton radiationless deactivation at the surface.[33] These effects are at present ill defined and not well understood for simple insulators. The effect of the surface as a sink for free excitons provides a central ingredient of our phenomenological approach. Our approach bears a formal analogy to the "dead layer" model originally advanced by Hebb[34] to explain exciton induced photoionization of F centers in alkali halides. To establish the relation between our dynamic approach and the phenomenological dead layer model we portray in Fig. 21 the local concentrations of free excitons calculated from our diffusion model for several values of k. Near the surface $n(x)$ is low, rising to a maximum value and then decreasing as $\exp(-\alpha x)$. Approximation of the steeply rising curve at low x by a step function (see Fig. 21),

$$\begin{aligned} n(x) &= 0, \qquad x < h \\ n(x) &= \alpha e^{-\alpha x}, \qquad x > h \end{aligned} \tag{4.17}$$

results in the basic assumption underlying Hebb's ap-

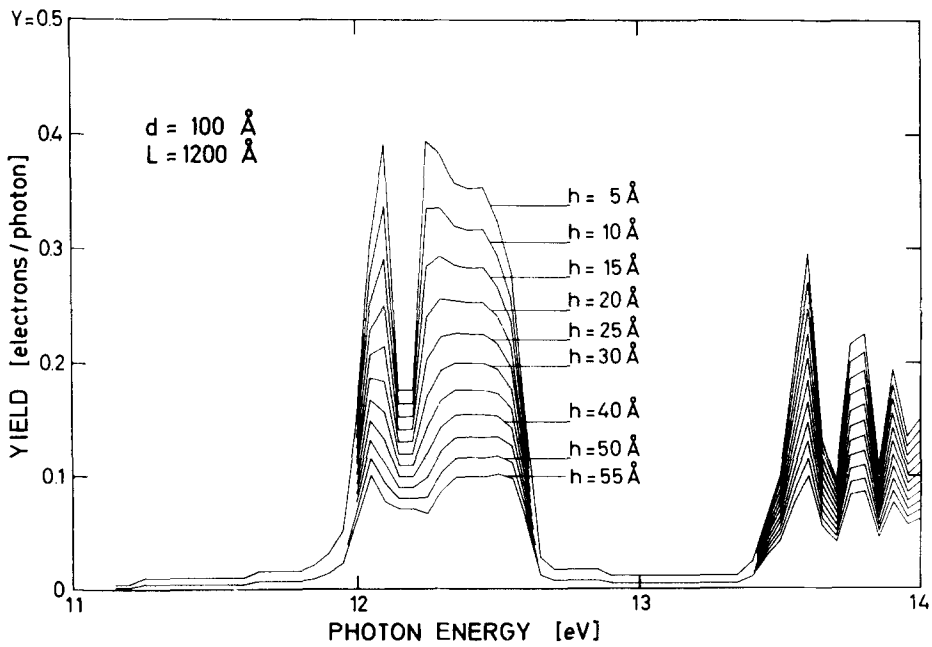

FIG. 24. The same as Fig. 23 but with a film thickness of 100 Å. The general shape corresponds well with the measurement but taking $h = 30$ Å from Fig. 23 the absolute values are too high by more than a factor of 2.

proach. Our diffusion model implies that the approximate cutoff h depends on the absorption coefficient; however, this dependence is not very strong, as is evident from Fig. 22. It is not surprising that the quantum yield

$$Y = S\tau[R]\frac{\alpha L}{\alpha L+1}\left\{\exp\left[-\frac{h}{L}(\alpha L+1)\right]-\exp\left[-\frac{d}{L}(\alpha L+1)\right]\right\} \tag{4.18}$$

for the dead layer model provides a semiquantitative description of our results. In Figs. 23 and 24 we present typical numerical data from Eq. (4.18), which provide a reasonable fit of our experimental data with $h \simeq 30$ Å, although we note that for small d values the dynamic approach is superior. Our dynamic approach is superior to the dead layer model because of two reasons. First, from the physical point of view we were able to provide a proper rationalization to the nature of the dead layer which provides only a crude approximation to the role of the surface on the reduction of the local concentration of free excitons near the boundary. We have to assume that free excitons do not exist only over a thickness which spans a single monomolecular layer, and not over a range of $h \simeq 20$–50 Å. Second, from the point of view of the solid state spectrocopist, if indeed surface effects were drastic so as to create a dead layer of thickness 20–50 Å, $h \sim k_{\max}^{-1}$ and the optical constants would be grossly modified, while our approach implies only minor modifications of the bulk optical properties by the boundary condition $n(o) = 0$. Third, our approach is more physical, demonstrating the nature of pertinent information extracted from photoionization yields on exciton dynamics in simple insulators.

Further extension of these studies to encompass a wide class of systems over the available temperature range will provide interesting information regarding exciton dynamics, exciton trapping lifetimes, and electronic relaxation between exciton states in "simple" insulators.

*Work supported by Deutsche Forschungsgemeinschaft DFG, Deutsches Elektronen–Synchrotron DESY, Hamburg, and by the Nerken Foundation at the Tel-Aviv University.

†Now at Deutsches Elektronen–Synchrotron DESY, Hamburg, Germany.

[1]For a recent review see U. Rössler, Band Structure and Excitons, in *Rare Gas Solids*, edited by M. K. Klein and J. A. Venables (Academic, New York, 1975).

[2]For a recent review, see B. Sonntag and R. Haensel, Dielectric and Optical Properties, in *Rare Gas Solids*, edited by M. L. Klein and J. A. Venables (Academic, New York, 1975).

[3]J. F. O'Brien and K. J. Teegarden, Phys. Rev. Lett. **17**, 919 (1966).

[4](a) N. Schwentner, M. Skibowski, and W. Steinmann, Phys. Rev. B 8, 2965 (1973); (b) E. E. Koch, V. Saile, N. Schwentner, M. Skibowski, W. Steinmann, and B. Raz, "Exciton Contribution to the Photoemission from Thin Films of Solid Argon," Jpn. J. Appl. Phys. (to be published) and preprint DESY SR-73/11 (Dec. 1973); (c) E. E. Koch, V. Saile, N. Schwentner, and M. Skibowski, Chem. Phys. Lett. 28, 562 (1974).

[5]J. T. Steinberger, E. Pantos, and J. H. Munro, Phys. Lett. **47A**, 299 (1974).

[6]Z. Ophir, B. Raz, and J. Jortner, Phys. Rev. Lett. 33, 415 (1974).

[7](a) M. A. Woolf and G. W. Rayfield, Phys. Rev. Lett. **15**, 238 (1965); (b) G. Mazzi, F. Toigo, and G. Torzo, J. Phys. C: Solid State Phys. **6**, 3652 (1973); (c) R. J. Loveland, P. G. Le Comber, and W. E. Spear, Phys. Lett. **39A**, 225 (1972); (d) B. Halpern, J. Lekner, S. A. Rice, and R. Gomer, Phys. Rev. **156**, 351 (1967).

[8]J. Roberts and E. G. Wilson, J. Phys. C: Solid State Phys. **6**, 2169 (1973).

[9]J. Jortner, L. Meyer, S. A. Rice, and E. G. Wilson, J. Chem. Phys. **42**, 4250 (1965).

[10](a) A. Gedanken, B. Raz, and J. Jortner, J. Chem. Phys. **59**, 5471 (1973); (b) O. Chesnovsky, B. Raz, and J. Jortner, J. Chem. Phys. **57**, 4628 (1972).

[11]R. Brodmann, R. Haensel, U. Hahn, U. Nielsen, and G. Zimmerer, Chem. Phys. Lett. **29**, 250 (1974).

[12]M. Martin, J. Chem. Phys. **54**, 3289 (1971).

[13](a) L. Apker and E. Taft, Phys. Rev. **79**, 964 (1950); (b) as before, Phys. Rev. **81**, 698 (1951).

[14]Z. Ophir, B. Raz, U. Even, and J. Jortner, J. Opt. Soc. Am. **64**, 1175 (1974).

[15]N. Schwentner, thesis, University Munich (1974).

[16]E. E. Koch, and M. Skibowski, Chem. Phys. Lett. **9**, 429 (1971).

[17]A. Harmsen, Diplomarbeit, Hamburg (unpublished).

[18]R. S. Scharber, and S. E. Webber, J. Chem. Phys. **55**, 3985 (1971).

[19]A. Harmsen, E. E. Koch, V. Saile, N. Schwentner, and M. Skibowski, in *Vacuum Ultraviolet Radiation Physics*, edited by E. E. Koch, R. Haensel, and C. Kunz (Vieweg-Pergamon, 1974), p. 339.

[20]G. Baldini, Phys. Rev. **128**, 1562 (1962).

[21](a) U. Nielsen, DESY F41-73/2 (1973) internal report; (b) R. Klucker and U. Nielsen, Computer Phys. Commun. **6**, 187 (1973).

[22]G. Baldini, Phys. Rev. **137**, A508 (1965).

[23]J. G. Angus and G. C. Morris, Mol. Cryst. Liq. Cryst. **11**, 309 (1970).

[24]A. Gedanken, B. Raz, and J. Jortner, J. Chem. Phys. **58**, 1178 (1973).

[25](a) E. O. Kane, Phys. Rev. **127**, 131 (1962); (b) J. M. Ballantyne, Phys. Rev. B **6**, 1436 (1972).

[26]B. E. Springett, J. Jortner, and M. H. Cohen, J. Chem. Phys. **48**, 2720 (1968).

[27]W. B. Fowler, Phys. Rev. **151**, 657 (1966).

[28]W. H. Miller, J. Chem. Phys. **52**, 3563 (1970).

[29]A. B. Belov, J. Ya Fugol', and E. V. Savchenko, Solid State Commun. **12**, 1 (1973).

[30]Y. Toyozawa, Prog. Theor. Phys. **20**, 53 (1958).

[31]N. Schwentner, Z. Ophir, B. Raz, M. Skibowski, and J. Jortner "Extrinsic Photoemission from Pure Solid Rare Gases" (unpublished).

[32]O. Simpson, Proc. R. Soc. A **238**, 402 (1957).

[33]U. Fano, Phys. Rev. **58**, 544 (1940).

[34]M. Hebb, Phys. Rev. **81**, 702 (1951).

[35]N. Schwentner, F.-J. Himpsel, V. Saile, M. Skibowski, W. Steinmann, and E. E. Koch, "Photoemission from Solid Rare Gases: Electron Energy Distributions from the Valence Bands," preprint DESY SR-74/17 (Dec. 1974).